coatings

MDPI

Article

Investigating the Water Jet Erosion Performance of HVOF-Sprayed WC-10Co Coatings on 35CrMo Steel Utilizing Design of Experiments

Daniel C. Ribu [1,*], Rajamony Rajesh [2], Duraisamy Thirumalaikumarasamy [3], Chidambaram Seshadri Ramachandran [4], C. Ahamed Saleel [5], Abdul Aabid [6], Muneer Baig [6] and Bahaa Saleh [7]

1 Department of Mechanical Engineering, Noorul Islam Centre for Higher Education, Tamil Nadu 629180, India
2 Department of Mechanical Engineering, Rohini College of Engineering and Technology, Tamil Nadu 629401, India; rajesh1576@yahoo.co.in
3 Department of Mechanical Engineering, Government College of Engineering, Bargur 635104, India; tkumarasamy412@gmail.com
4 Department of Materials Science and Engineering, The State University of New York (SUNY) at Stony Brook, New York, NY 11794, USA; csrcn1@gmail.com
5 Department of Mechanical Engineering, College of Engineering, King Khalid University, Abha 61421, Saudi Arabia; ahamedsaleel@gmail.com
6 Department of Engineering Management, College of Engineering, Prince Sultan University, Riyadh 11586, Saudi Arabia; aaabid@psu.edu.sa (A.A.); mbaig@psu.edu.sa (M.B.)
7 Department of Mechanical Engineering, College of Engineering, Taif University, Taif 26432, Saudi Arabia; bahaa_saleh69@yahoo.com
* Correspondence: ribucdaniel@gmail.com

check for updates

Citation: Ribu, D.C.; Rajesh, R.; Thirumalaikumarasamy, D.; Ramachandran, C.S.; Ahamed Saleel, C.; Aabid, A.; Baig, M.; Saleh, B. Investigating the Water Jet Erosion Performance of HVOF-Sprayed WC-10Co Coatings on 35CrMo Steel Utilizing Design of Experiments. *Coatings* **2022**, *12*, 482. https://doi.org/10.3390/coatings12040482

Academic Editor: László A. Péter

Received: 14 December 2021
Accepted: 18 March 2022
Published: 2 April 2022

Abstract: To enhance the surface of a material with the desired qualities for diverse applications in service, a variety of thermal and thermo-chemical surface treatment processes are used. Due to the high-velocity impact inherent in the process, high-velocity oxy-fuel (HVOF) spray is now frequently employed in industrial applications for its ability to generate a high-quality coating with appropriate hardness and low oxide content. In this investigation, a high-velocity oxy-fuel (HVOF) thermal spraying process was utilized to coat WC-10Co powders on a 35CrMo steel substrate. A water jet erosion test was also used to examine the substrate and coated samples' erosion behavior. The erosion rate was systematically investigated using water jet variables such as the angle of impingement, water jet velocity, standoff distance, and erodent discharge. For the development of multiple regression models, experiments were performed utilizing the central composite rotatable design and the response surface methodology. The angle of impingement had the most impact on the rate of coating erosion, leading to the water jet velocity, standoff distance, and erodent discharge.

Keywords: WC-10Co coating; high-velocity oxy-fuel (HVOF); erosion rate; stainless steel; response surface methodology

1. Introduction

Material deterioration due to erosion and oxidation in high-temperature environments is a major cause of wear in power plants, aircraft engines, and petrochemical industries. Erosion is a common cause of failure in complex industrial machinery, ships, hydroelectric power plants, drilling, and other sectors [1–3]. The predominant categories of erosion that can occur depending on the fluid medium are sandblasting erosion, droplet erosion, slurry erosion, and cavitation erosion [4]. Equipment and component failures, for instance hydraulic turbine parts, mud pumps, and drill pipes, are frequently caused by slurry erosion [5]. To reduce the cost and service life loss, it should be diagnosed and prevented early on. It is described as the structural parts' wear (primarily hydrodynamic turbine

blades, penstocks, labyrinth seals, needles, spears, and casings) caused by the flow stream of the solid particles striking the target region at a greater velocity [6–8]. The deterioration of the tribological performance in high-temperature environments such as the ones in boilers and super-heaters is a significant problem that leads to premature failure. This leads to financial loss and machinery downtime for a range of industries, adding significantly to their operating cost [9–13]. Generally, the most influential tribological properties that dictate the high-temperature wear of materials is their erosion and oxidation resistance. Slurry erosion is often noticed in diverse equipment including reamers, hoppers, mud pumps, and blades [14,15] and is a primary source of dredging engineering component losses. The problem is exacerbated for equipment used in the ocean since the corrosive environment of seawater can cause substantial equipment destruction owing to corrosion-expedited erosion [16]. As slurry erosion occurs exclusively on the surface, surface treatment is an effective approach for enhancing slurry erosion performance.

The high-pressure water jet method [17–19] is a revolutionary surface-treatment technology that uses the water jet's ultra-high impact kinetic energy to achieve polishing, cutting of the material, and surface cleaning. Water jet technology has been utilized in industries [20,21], such as for pumping, rock breaking, mining, cleaning of ships, removal of rust, and material cutting [22,23], due to its greater efficiency, broad applicability, and environmental friendliness. The simulation of flow fields has made great progress [24,25]. To reduce erosion rates, various surface engineering methods have been developed. Thermal spray methods, in particular air plasma spray (APS) and high-velocity oxy-fuel (HVOF) techniques, have piqued researchers' interest due to their ability to create superior WC-based erosion-resistant coatings [26]. In a number of studies, WC-Co cermet coatings sprayed by HVOF were found to exhibit excellent hardness, toughness, and anti-wear properties [27]. HVOF spray is an efficient technique for the deposition of cermet coatings to eliminate slurry erosion due to its great qualities such as greater velocities and lower flame temperature compared to the plasma spraying technique [28,29], and as a result, WC degradation is prevented and the microstructural characteristics of the coatings are enhanced [30]. Furthermore, the HVOF technique is a diverse approach with the benefits of the outstanding quality of the coating and superior bonding strength [31]. Numerous researchers have explored the erosion and corrosion performance of WC cermet coating on steels by utilizing different thermal spray methods [32–34]. Daniel C. Ribu et al. investigated the slurry erosion performance of HVOF-sprayed coatings. The authors reported that rotational speed was the most significant parameter determining the mass loss of the coatings followed by the angle of impingement, slurry composition, and time [35]. Ahmed et al. found that WC-Co coatings produced by the S-HVOF technique showed lower corrosion resistance compared with the coatings produced by the HVOF-JK and HVOF-JP techniques, most probably due to strong carbon loss during spraying, leading to the presence of metallic tungsten and the presence of a higher amount of amorphous/nanocrystalline constituents compared with conventional coatings [36]. Pengbo Mi et al. investigated the composition, microstructure, mechanical properties, and wear performance of the as-sprayed and heat-treated WC-Co coating. The results showed that, after heat treatment, the coating showed a dense microstructure and the maximum hardness after heat treatment at 450 °C [37]. However, there are not very many studies on the water jet erosion performance of WC-Co-coated steels using the HVOF spray technique. Accordingly, the current investigation aimed to evaluate the water jet erosion performance of WC-10Co coatings on 35CrMo steels using HVOF spray in a real boiler environment.

2. Experimental Work

WC-10Co powders were deposited on a 35CrMo steel base material surface with a 200 µm thickness using the HVOF spray equipment available at Annamalai University in India (HIPOJET-2700, Make: Metallizing Equipment Co., Jodhpur, India). The thickness of the substrate was 5 mm. After that, a digital micrometer (Mitutoyo, Kanagawa, Japan, precise to 0.001 mm) was utilized to estimate the coating thickness for every normal operating

circumstance. The thickness of the deposition was achieved by changing the passes utilized for coating. Figure 1a represents the high-velocity oxy-fuel spray equipment. The coated specimens are shown in Figure 1b. Prior to spraying, the base material was preheated at 0.8 m/s through one complete torch cycle, attaining 120–180 °C. The dimensions of the samples utilized for this study were15 mm × 10 mm × 8 mm, with edges 1 mm longer and a 45° chamfering. Acetone was utilized to wash and ultrasonically clean the specimens. The base material surface roughness was improved using corundum (size of 320 ± 500 µm).

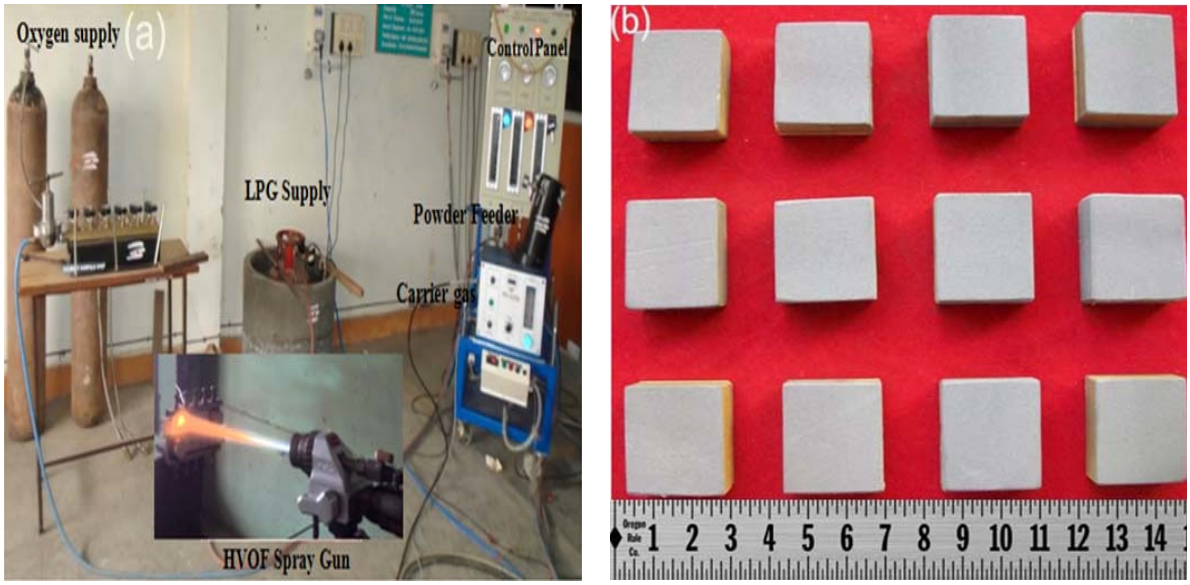

Figure 1. Experimental details: (**a**) HVOF spraying facility; (**b**) coated specimens.

After grit blasting, the surface roughness of the base material was found to be 5–10 µm using a surface roughness instrument (Make: Mitutoyo, Japan; Model: Surf test 301). The conventional powders had the following composition: WC-90 weight percentage and Co-10 weight percentage. The particle size ranged from 15 to 45 µm. The process parameters of WC-10Co utilizing HVOF can be seen in Table 1.

Table 1. HVOF process parameters.

Process Parameters	Range
Oxygen flow rate	253 lpm
LPG flow rate	61 lpm
Powder feed rate	35 g/min
Spray distance	227 mm

2.1. Coatings' Characterization

A scanning electron microscopy study (Make: JEOL, Tokyo, Japan; Model: 6410-LV) was performed to examine the surface characteristics and morphologies of the powder and coatings. Figure 2a depicts a Scanning Electron Microscopy SEM view of the as-coated powder with a spherical form with particle sizes of −45 + 15 µm. The melting performance and flow capacity were improved by the narrow particle size dispersion and spherical powders.

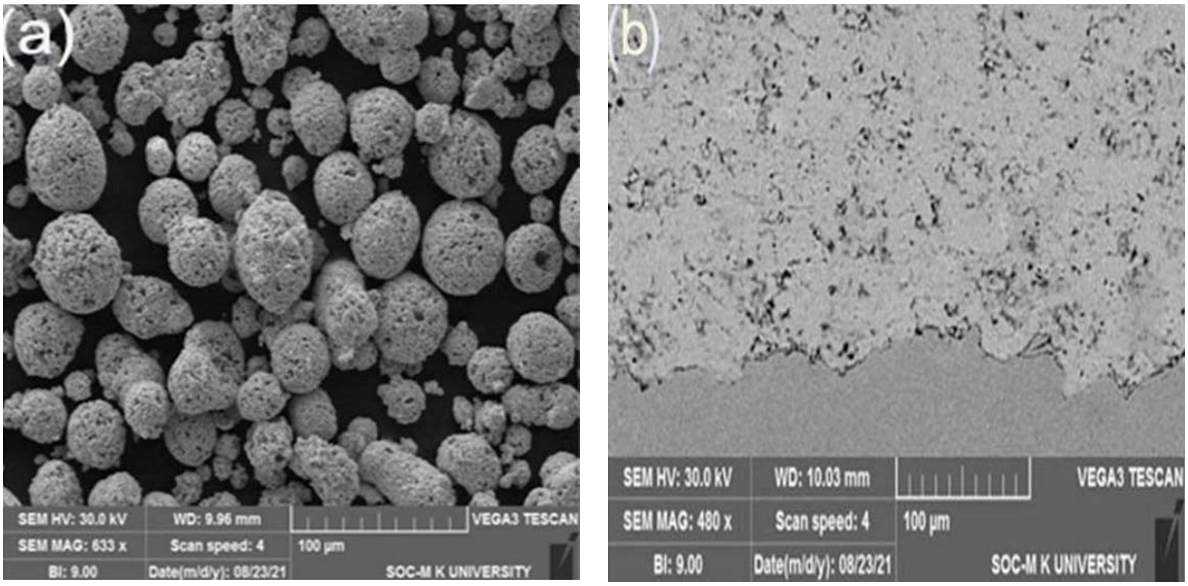

Figure 2. SEM micrographs of the WC-10Co powder and coatings. (**a**) WC-10Co powder; (**b**) WC-10Co coating.

The SEM micrographs revealed that the coating was relatively thick and had excellent adhesion with the uncoated substrate, as seen in Figure 2b. This means that the coating adhered well to the surface of the base material owing to the high velocity of the thermal spray. The Energy-dispersive X-ray spectroscopy EDS analysis of the powder and coating is shown in Table 2. The bond strength of the coating was found to be 18 MPa. In general, the amount of pores produced in the coatings via HVOF was very low. This was the cause for the higher density and high cohesive strengths of the different coatings owing to the higher impact velocity of the coating elements. The porosity data were obtained utilizing optical microscope equipment (Make: Meiji; Saitama, Japan, Model: MIL-7100) with microstructure processing software (Metal Vision Version 6) on metal lographically generated cross-sections of coatings following ASTM B 276 [38]. In this analytical procedure, the images collected under 1000× magnification using optical microscopy were chosen for porosity examination to reveal open pores and regular cracks. A 400 µm square region of the coating was examined. At five random locations, the same procedure was followed to reveal the average volume of the pores as a percentage. The porosity level of the coating was 2 vol.%. A micro-hardness measurement (Make: Shimadzu; Kyoto, Japan) was performed to determine the coating's micro-hardness. Model: HMV-2T) with a 2.94 N load and a 15 s holding time. The hardness of the specimens was assessed at ten places on the coating cross-section. The fracture toughness of the coating was determined utilizing the HV-5 Vickers hardness method, which used the indention method on the coating cross-section with a 49 N load and a 15 s holding time, and the mean average value of twenty trials gave the effective fracture toughness. The hardness observed at the cross-section of the coated sample was 1120 HV. Figure 3 illustrates the pictures, which were assessed utilizing image processing software. Figure 3b represents the pores of various sizes. Figure 3c demonstrates the color-coded overlay image for pore identification. The bonding capability of the coatings was monitored in accordance with ASTMC-633-01 [39]. The deposition layer was bonded to the 35CrMo steel using E7 adhesive. Following solidification, a universal tensile test apparatus (FIE Blue Star; Maharashtra, India) was utilized to determine the material strength. The evaluation was performed with a UNITEK-94100 model. The crosshead speed of the apparatus was 1 mm/min. The coating bond strength was estimated using an average of three experimental results. The Atomic Force Microscopy AFM analyses of the eroded specimens were performed by means of Si probes (Make: JPK, London, UK. Model: Nano Wizard II) operated in non-tapping mode.

Table 2. EDS analysis of the WC-10Co powder and coatings.

Element	Wt.%	At.%	Element	Wt.%	At.%
W K	87.32	68.13	**W K**	85.66	64.21
Co K	9.10	21.98	**Co K**	9.47	24.58
C K	3.58	9.91	**C K**	4.87	11.61
Total	100	-	**Total**	100	-
(**a**) WC-10Co powder			(**b**) WC-10Co coating		

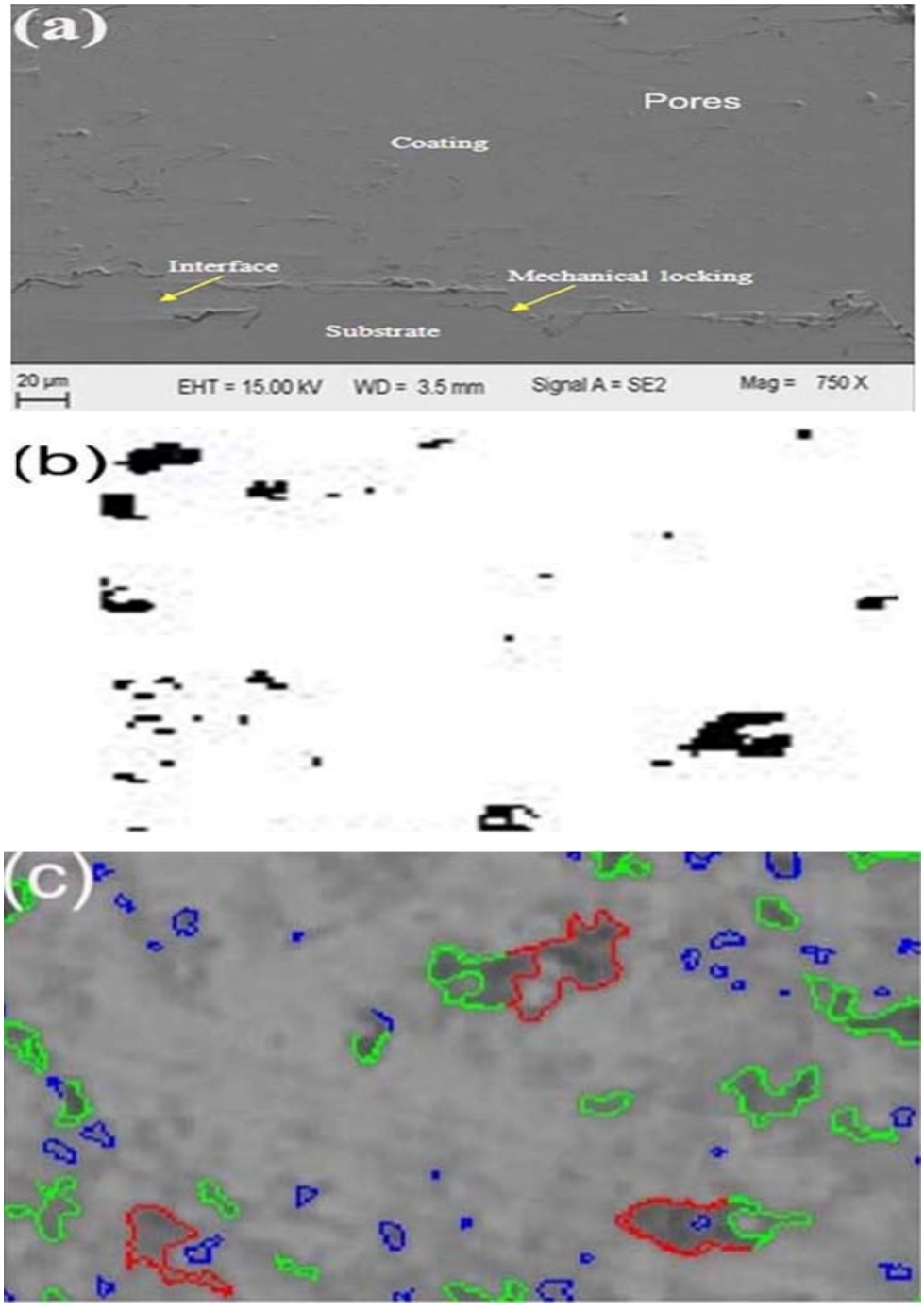

Figure 3. Porosity analysis. (**a**) Cross sectional image; (**b**) Binary image; (**c**) Color coded image.

2.2. Water Jet Erosion Investigation

The coated and uncoated specimens' mass loss was examined using a water jet erosion apparatus (Model: TR-411, Make: DUCOM, Bangalore, India) based on the ASTM G75-07 standard [40] to study the impact of angle of impingement, water jet velocity, standoff distance, and erodent discharge on the erosion behavior. The experiment was conducted by weighing the specimen before and after the process to determine the loss of mass. Figure 4a shows the water jet erosion setup. The uncoated and coated specimens after the water jet erosion test are shown in Figure 4b,c. Specimens were polished and ultrasonically cleaned using acetone and weighed prior to the test and post-test to find the weight loss, from which the erosive wear was calculated. The sample to be analyzed was cleaned properly before being weighed in precision weighing equipment. With the use of clamps, these standard-sized specimens were attached to the disc at the desired radial distance. The disc was dipped into the slurry in the container, together with the specimen. The specimens were then rotated at the specified speed for a set period of time after the motor had started. The specimen was removed, washed, and weighed once the experiment was complete. The rate of erosion was calculated at the rate of the loss of mass with respect to various experimental parameters. In the water jet experiments, 50 µm quartz sand was utilized as the erodent, and its micrograph can be seen in Figure 5.

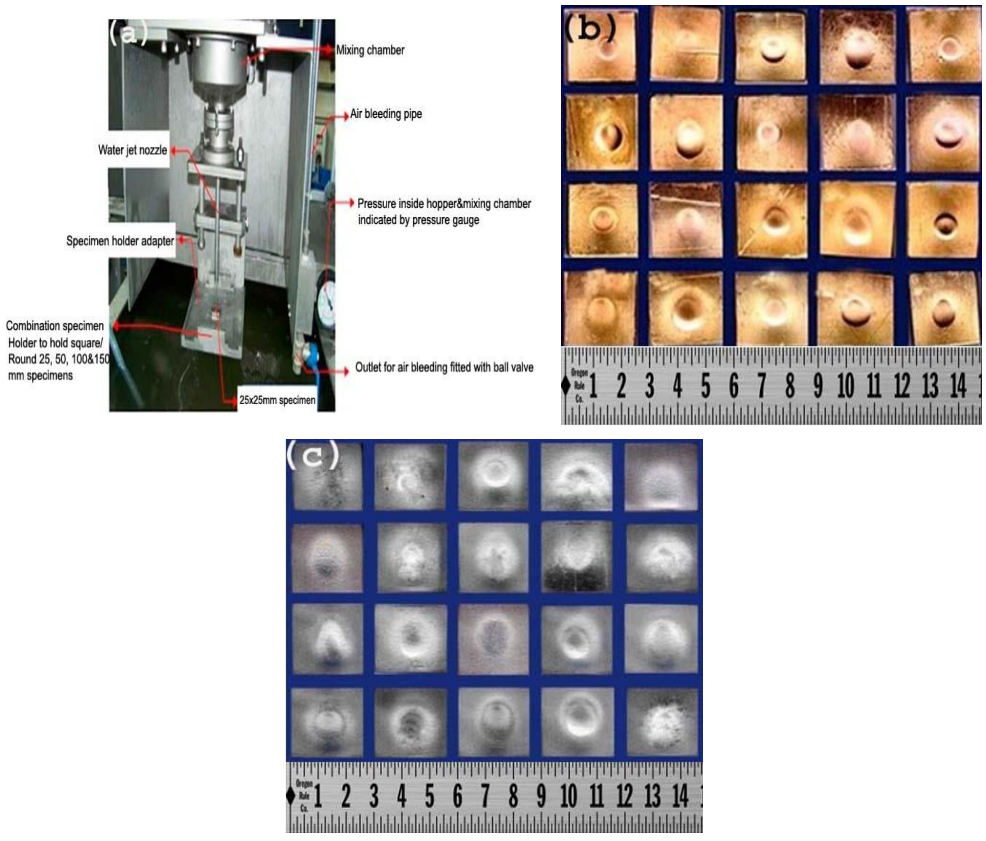

Figure 4. Photographs of water jet erosion specimens before and after the test: (**a**) water jet erosion test setup; (**b**) uncoated specimens after the test; (**c**) coated specimens after the test.

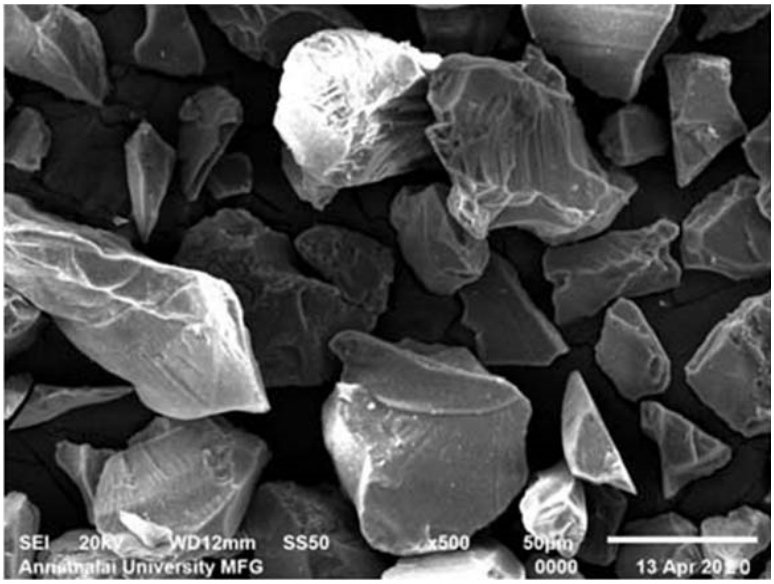

Figure 5. SEM micrograph of the erodent particles.

2.3. Formulating the Experimental Design Matrix to Conduct the Erosion Tests

After examining all of the possible ranges of the water jet erosion testing parameters, their limits were determined such that the erosive experiment could be carried out with ease. A central composite rotatable model of second order (RSM) was utilized to establish the empirical relationship between the variables using as few experiments as possible while sacrificing the accuracy [41]. Table 3 lists the variables and their ranges that were examined for the erosion test. The experimental findings of the water jet erosion tests for both the coated and untreated stainless steel are given in Table 4.

Table 3. Water jet erosion test parameters and their levels.

S. No.	Factors	Notations	Units	Levels				
				−2	−1	0	1	2
1	Angle of impingement	A	deg.	35	50	65	80	95
2	Water jet velocity	V	m/s	10	20	30	40	50
3	Standoff distance	D	mm	30	35	40	45	50
4	Erodent discharge	F	gpm	500	1000	1500	2000	2500

Table 4. Experimental design matrix and results.

Exp. Condition	Variables (Factors)				Responses	
	Angle of Impingement (A) Deg	Water Jet Velocity (V) m/s	Standoff Distance (D) mm	Erodent Discharge (F) gpm	Mass Loss of Uncoated Substrate (g)	Mass Loss of Coatings (g)
1	45	20	40	1000	0.0594	0.0223
2	75	20	40	1000	0.0881	0.033
3	45	40	40	1000	0.2603	0.0976
4	75	40	40	1000	0.2689	0.1008
5	45	20	50	1000	0.0841	0.0315
6	75	20	50	1000	0.0986	0.037
7	45	40	50	1000	0.2604	0.0977
8	75	40	50	1000	0.2884	0.1082
9	45	20	40	2000	0.0381	0.0143
10	75	20	40	2000	0.0434	0.0163

Table 4. *Cont.*

Exp. Condition	Variables (Factors)				Responses	
	Angle of Impingement (A) Deg	Water Jet Velocity (V) m/s	Standoff Distance (D) mm	Erodent Discharge (F) gpm	Mass Loss of Uncoated Substrate (g)	Mass Loss of Coatings (g)
11	45	40	40	2000	0.2104	0.0789
12	75	40	40	2000	0.2613	0.098
13	45	20	50	2000	0.0589	0.0221
14	75	20	50	2000	0.0773	0.029
15	45	40	50	2000	0.2197	0.0824
16	75	40	50	2000	0.2894	0.1085
17	30	30	45	1500	0.1042	0.0391
18	90	30	45	1500	0.1411	0.0529
19	60	10	45	1500	0.0131	0.0049
20	60	50	45	1500	0.3687	0.1383
21	60	30	35	1500	0.1302	0.0488
22	60	30	55	1500	0.1718	0.0644
23	60	30	45	500	0.2103	0.0789
24	60	30	45	2500	0.1869	0.0701
25	60	30	45	1500	0.1312	0.0492
26	60	30	45	1500	0.1348	0.0506
27	60	30	45	1500	0.1295	0.0486
28	60	30	45	1500	0.1307	0.049
29	60	30	45	1500	0.1247	0.0468
30	60	30	45	1500	0.1361	0.051

3. Predictive Statistical Model for the Erosion Rate

In this research, a linear quadratic empirical correlation was established to estimate the responses depending on the experimentally determined values in order to correlate the input variables to the wear rate. The angle of impingement (A), water jet velocity (V), standoff distance (D), and erodent discharge are all factors that influence the responses (F). It can be described as follows:

$$\text{Responses} = f(A, V, D, F) \quad (1)$$

The regression coefficients were determined utilizing the Design Expert V 8.1 statistical software in this investigation. The final empirical correlations were made utilizing these coefficients following the identification of the factors that were noteworthy (with a 95% confidence level). The following are the final empirical equations for assessing the wear rate:

$$\text{Mass loss of uncoated substrate (gpm)} = \{0.23 - 0.038\,(A) - 0.7 \times 10^{-3}\,(V) - 0.039\,(D) - 0.025\,(F)\} \quad (2)$$

$$\text{Mass loss of coatings (gpm)} = \{0.029 + 4.14 \times 10^{-3}\,(A) + 6.4 \times 10^{-3}\,(V) + 8.4 \times 10^{-3}\,(D) - 2.7 \times 10^{-4}\,(F)\} \quad (3)$$

Confirming the Adequacy of the Empirical Correlations Established

In this study, the appropriateness of the obtained empirical correlations was assessed using the analysis of variance (ANOVA) method. Tables 5 and 6 display the findings of the ANOVA studies on the resistance to erosion of the uncoated and coated substrates, respectively. In the literature, there is a procedure for evaluating ANOVA findings [42]. The angle of impingement, jet velocity, standoff distance, and erodent discharge were the leading variables that had a direct impact on the responses as per the priority, according to the F-value evaluation. The model's goodness-of-fit is shown by the coefficient of determination R^2. According to the ANOVA findings, the established model was significant, whereas the lack of fit was not significant. As a consequence, the established correlations

could be efficiently used to estimate the responses by replacing the experimental input variables in coded form, as requested.

Table 5. ANOVA results for the uncoated stainless steel.

Source	Sum of Squares	df	Mean Square	F-Value	*p*-Value Prob > F	Title
Model	3.105×10^{-3}	4	7.763×10^{-4}	48.81	<0.0001	Significant
Angle of impingement	1.862×10^{-3}	1	1.862×10^{-3}	117.10	<0.0001	-
Jet velocity	8.777×10^{-4}	1	8.777×10^{-4}	55.18	<0.0001	-
Standoff distance	4.461×10^{-4}	1	4.461×10^{-4}	28.05	<0.0001	-
Erodent discharge	1.050×10^{-5}	1	1.050×10^{-5}	0.66	0.4243	-
Residual	3.976×10^{-4}	25	1.590×10^{-5}	-	-	-
Lack of fit	3.468×10^{-4}	21	1.651×10^{-5}	1.30	0.4431	Not significant
Pure error	5.085×10^{-5}	4	1.271×10^{-5}	-	-	-
Core total	3.503×10^{-3}	29	$R^2 = 0.9987$	-	-	-

df: degrees of freedom: CV: coefficient of variation; F: Fisher's ratio; p: probability.

Table 6. ANOVA results for the coated stainless steel.

Source	Sum of Squares	df	Mean Square	F-Value	*p*-Value Prob > F	Title
Model	3.036×10^{-3}	4	7.589×10^{-4}	1419.81	<0.0001	Significant
Angle of impingement	1.840×10^{-3}	1	1.840×10^{-3}	3441.47	<0.0001	-
Jet velocity	9.346×10^{-4}	1	9.346×10^{-4}	1748.42	<0.0001	-
Standoff distance	4.067×10^{-4}	1	4.067×10^{-4}	760.87	<0.0001	-
Erodent discharge	2.396×10^{-6}	1	2.396×10^{-6}	4.48	0.0444	-
Residual	1.336×10^{-5}	25	5.345×10^{-7}	-	-	-
Lack of fit	1.286×10^{-5}	21	6.125×10^{-7}	4.90	0.0667	Not significant
Pure error	5.000×10^{-7}	4	1.250×10^{-7}	-	-	-
Core total	3.049×10^{-3}	29	$R^2 = 0.9942$	-	-	-

df: degrees of freedom: CV: coefficient of variation; F: Fisher's ratio; p: probability.

4. Results and Discussion

4.1. Influence of the Impact Angles on the Erosion Rate

At lower impact angles, the erodent particle might have a propensity to slide along the surface, ploughing the material as it does so, as seen in Figure 6a. The material would be eliminated from the surface by the subsequent sliding of the particle; in other words, in a ploughing action, a portion of the volume pushed aside at lower angles of incidence can become warped and moved. The wear rate was substantially higher because the erodent particles were in contact with the surface for a long time during sliding. The eroded scars varied in length and shape owing to the variation of the sand particles' impingement angles. However, a small rubbing action was observed on the coated surface at low impingement angles, which removed a small volume of the material, as shown in Figure 6b. The micro-cutting and wedges are seen in the Figure 6c. Such a pattern can be seen in the ductile metallic material when viewed at moderate angles.

Both ejection and lamellae plastic deformation play a significant role in erosion degradation at shallow impingement angles. Grooves or plough markings are also prominent in the plastically deformed regions. The plastic grooves resemble scratches left on the surface of the coating by a sharp and firm indenter in several circumstances, and they typically follow the particle-colliding direction. Ejection is generated by grain lamellar micro-cracking and plastic deformation accompanied by spreading of the deformed material, as observed in Figure 6d in the circumstance of eroded surfaces with a shallow angle. The mechanism by which material is removed from a surface upon erosion attack can be either ductile or brittle. The ductile process (stainless steel) is characterized by the highest waste at lower impact angles in general. This mechanism can degrade the majority of metallic materials [43].

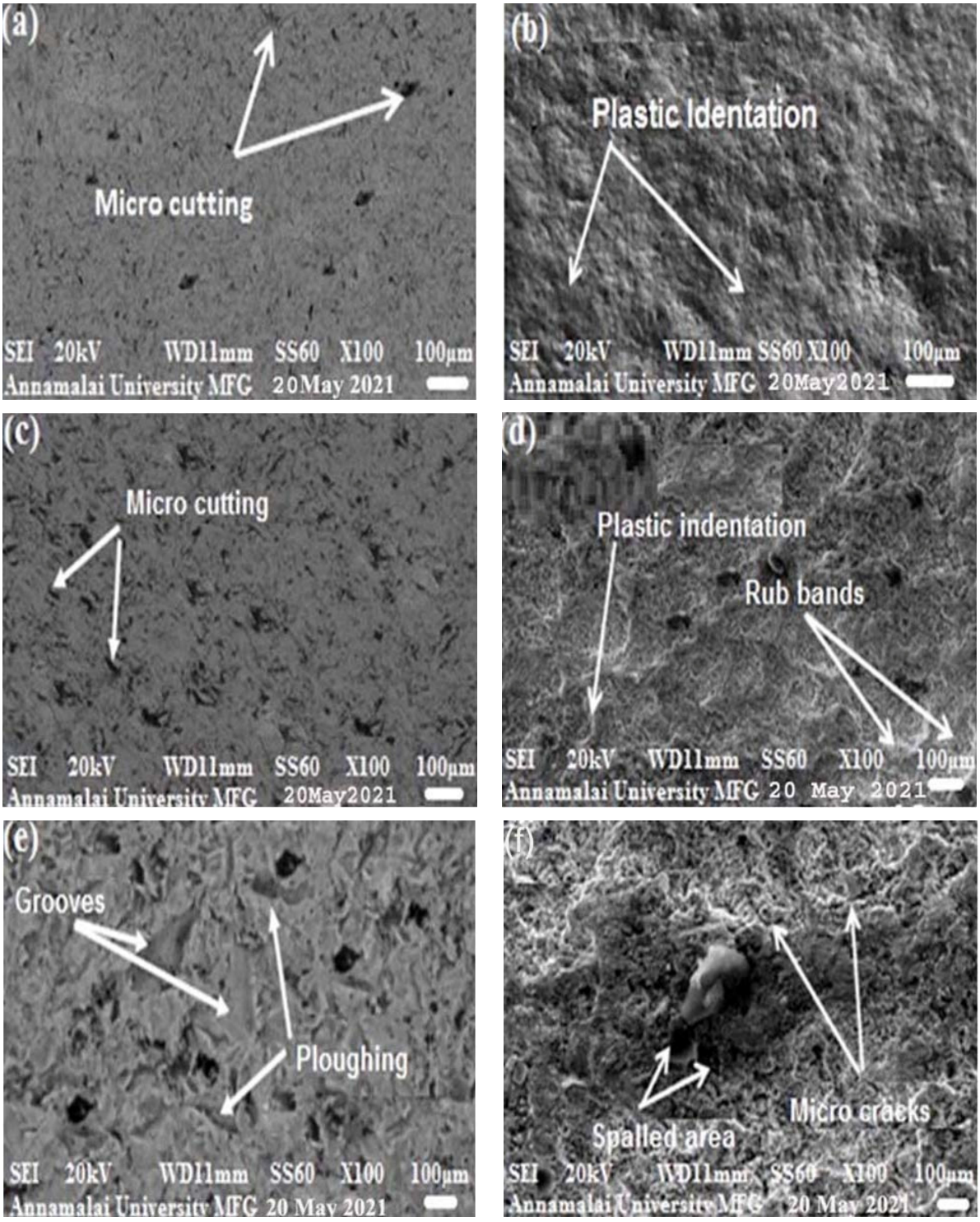

Figure 6. Worn surfaces of the coatings and substrate under different impact angles: (**a**,**c**,**e**) uncoated substrate; (**b**,**d**,**f**) coatings.

Metals impacted at higher angles experience drilling-like cutting actions. Hence, the het hits the target surface with particles, forming small lips and plates in eroded uncoated stainless steel, as shown in Figure 6e. For brittle (WC-1-coated stainless steel) ceramic materials, on the other hand, the process of erosion is characterized by maximum losses at higher angles of impact, during which erosion happens through cracking and chipping of the surface material [44].

When a particle strikes a metal surface, the response of this material can be elastic or plastic deformation, depending mainly on its yield strength. According to Hutchings (1979) [45], one way to know the extent of damage caused by the impact of a particle on a ductile material is to estimate it using the best or Metz number (B), given by Equation (1).

$$B = \rho \times V^2 / \sigma_Y$$

where:

B = best or Metz number (dimensionless);
ρ = density of the target material (Mg/m^3);
V = particle impact velocity (m/s);
σ = yield strength of the target material (MPa).

Because a higher porosity level of the coating is frequently seen along lamella boundaries, it can affect the inter-lamella strength and also induce micro- and macro-cracking, which can result in lamellae loss and, therefore, removal of the coating. The material is removed from the surface by breaking the boundaries and pulling them out near the grooves. Fragmented lamellae and fragmentation, as well as massive craters were observed on the eroded surfaces of the eroded region (Figure 6f).

4.2. Influence of the Water Jet Velocity on the Erosion Rate

As the water jet's velocity diminished, the kinetic energy imparted to the particle lowered. Once the kinetic energy is lower, a single impact would provide a good result (reduced erosion). Furthermore, as seen in Figure 7a, the particle jet divergence developed at low velocities, promoting micro-cutting in the uncoated stainless steel. Because the particle still had a significant horizontal velocity component when it departed from the metal surface, the initial impact energy was expended in the deformation [46]. Even as the impact energy reduced, fewer lateral cracks formed surrounding the plastic indentation on the carbide coatings' lamellae, as shown in Figure 7b. In medium jet velocity conditions, a moderate impact energy provided to the particles was able to promote micro-cutting in the stainless steel. As can be seen in Figure 7c,d, the particle's reduced forward momentum in the uncoated and coated stainless steel implied that it would roll over the target surface, leading to less surface deformation and rub bands. As a result, material removal would be limited in low and medium jet velocity circumstances. The rate of erosion improved as the starting velocity of the jet increased. This demonstrates that the rate of erosion is closely proportional to the square of the particle's kinetic energy. Though perhaps not conclusive, this could be because, as seen in Figure 7e, broader areas were eliminated underneath the higher velocity jet impact. Increased plasticity at higher velocity may enhance the loss erosion of brittle materials due to irreversible deformation, which increases the driving forces for lateral cracking and, hence, reduces the resistance to future impacts [47]. One could expect the shear force applied by the particle to increase as the contact velocity increases. With increasing velocity, the jet divergence likewise decreased. As a result, during the impact, additional material should be moved from beneath the particle towards the front of the crater [48]. The extensive lateral cracking observable at individual impact sites, as well as the indications of plastic indentation, as illustrated in Figure 7f, agreed with this. As a result, the potential of a plastic response to erosive impact as a result of higher surface temperatures could unintentionally contribute to more lateral spallation.

4.3. Influence of the Standoff Distance on the Erosion Rate

The standoff distance was found to have a lesser impact on the rate of metal removal. The kind of jet striking on the coating is determined by the standoff distance, which might be continuous, impact, or mixed. Lower material removal rates at a lower standoff distance are related to the decrease in pressure of the nozzle as the distance decreases, while a drop in the rate of material removal at a higher standoff distance is due to a decrease in the jet velocity as distance increases [49].

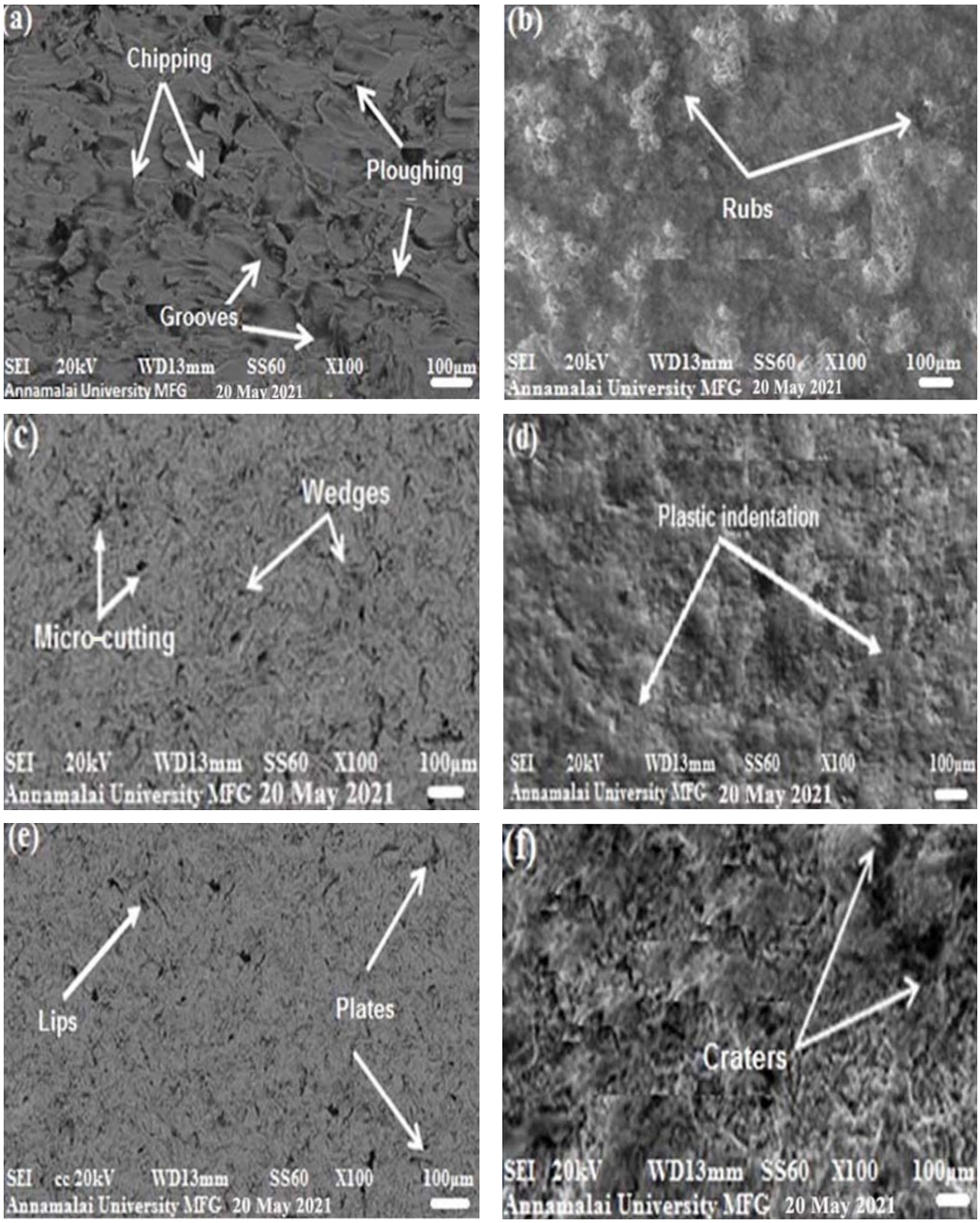

Figure 7. Worn surfaces of the coatings and substrate at different water jet velocities: (**a**,**c**,**e**) uncoated substrate; (**b**,**d**,**f**) coatings.

Once the sample is closer to the nozzle, the erosion pattern can resemble a butterfly pattern in the initial few seconds of contact. The target under the jet is not corroded in the center, but there is considerable erosion along the boundaries of the jet diameter, where a grain will be subjected to intense lateral jet flows, and it will experience large pressure differences throughout its width. The removal of material from the target stainless steel surface by the micro-cutting and metal cutting features observed on the eroded surfaces can be inferred from Figure 8a–e.

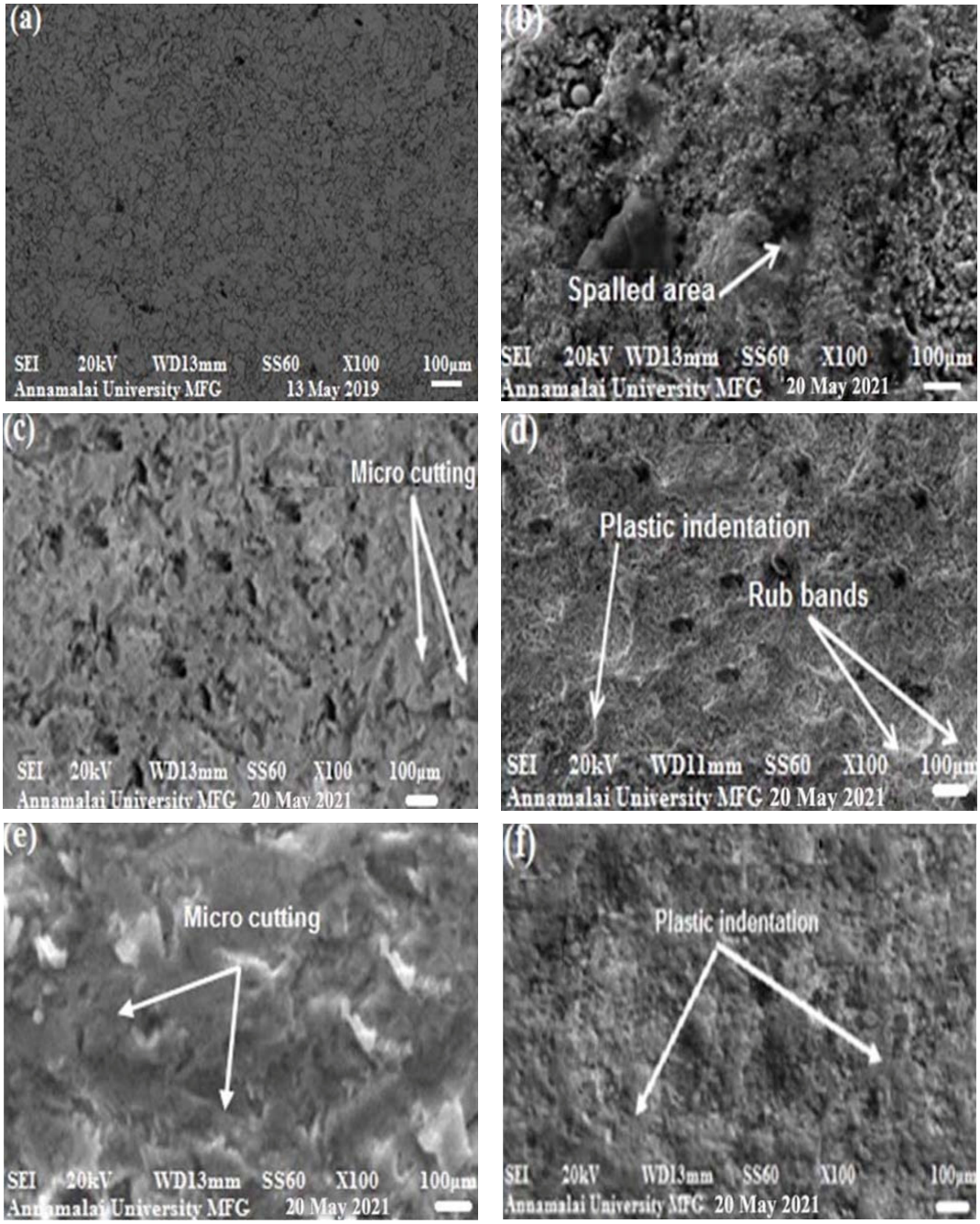

Figure 8. Worn surfaces of the coatings and substrate at different standoff distances: (**a**,**c**,**e**) uncoated substrate; (**b**,**d**,**f**) coatings.

Because the velocity magnitude dropped as the standoff distance increased, fine particles wandered more at lower standoff distances because the jet radial velocity was higher. The former circumstance had a stronger influence at a standoff distance of 45 mm than at a standoff distance of 55 mm since more tiny particles deviated in the former scenario. It is important that when the standoff distance decreases, the static pressure on the substrate increase, resulting in a higher percentage of deviated tiny particles. The slope of the curve increase as the standoff distance is increased to 35 mm, and the substrate erodent increases. Micro-cutting and metal cutting features were observed on the eroded surfaces.

4.4. Influence of Erodent Discharge on the Erosion Rate

Figure 9 demonstrates the influence of erodent discharge on the substrate's erosion scar and the as-treated sample. The particle mass hitting the target region per unit area per unit time is commonly referred to as erodent discharge. Erosion rates grow in a nonlinear relationship with rising erodent discharge and diminish as the angle of impingement increases. Increases in erodent discharge, on the other hand, have an influence on the shape of the crater and the effect of particles on the resistance to wear. Figure 9 exhibits SEM images of eroded samples, demonstrating the failures of micro-cutting, ploughing, and platelets caused by erodent particles interacting with the target surface.

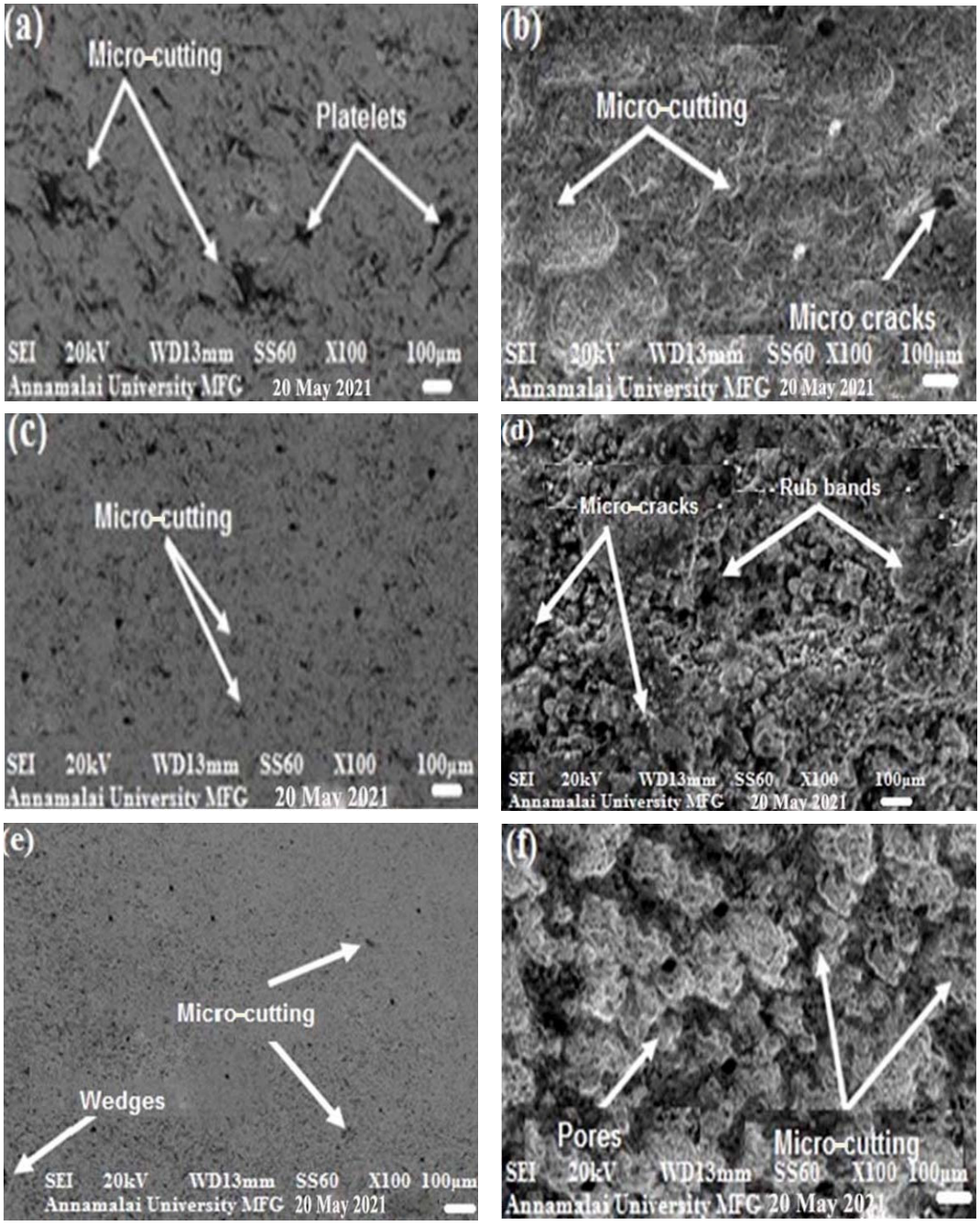

Figure 9. Worn surfaces of the coatings and substrate at different erodent discharges: (**a**,**c**,**e**) uncoated substrate; (**b**,**d**,**f**) coatings.

For lower erodent feed rates, the incident energy (impact energy) increased. The erosion quantity destruction per unit mass of abrasive hitting the target increased once the erodent discharge at impact decreased. Once the erodent discharge was lower, the mean free path of the water jet erodent particles was significantly longer, and thus, the risk of impact between the rebounding particles and the incident particles was remarkably low. The incidence of erosion increased significantly as the concentration of particle dropped, increasing the conveying velocity. Hydrodynamic particle interactions in the nozzle established as the erodent discharge increased, and these interactions became more noticeable as the erodent discharge increased. Even as the flux increased, the chance of particle collisions grew dramatically, and hence, the rate of erosion should decrease [50,51]. This turbulence reduction increased the water jet's spreading rate and encouraged a speedier decline of the jet's mean centerline velocity, minimizing the erosion. According to the SEM micrographs, the substrate had plough markings, micro-cutting, and the formation of wedges, as can be seen in Figure 9a,c,e. In the WC-10Co coatings, cracking, ejections, and lamellae spallation were found (Figure 9b,d–f). The rate of erosion was much lower at the maximum concentrations of particles compared to the lower flux circumstances, as seen by the water jet erosion experiment. It could be observed that higher particle concentrations resulted in more inter-particulate and particle–wall collisions.

5. AFM Analysis

The material removal of stainless steel examined at a 30° impact angle was higher than the removal of stainless steel measured at a 90° impact angle. This type of erosion is common in ductile materials. At a severe angle ($\alpha = 90°$), however, all of the coatings degraded more than at a shallow angle ($\alpha = 30°$). Brittle materials are known for their brittle characteristics. Figure 10a shows the images taken at the eroded surface at low impingement angles. The AFM images of the eroded surfaces at higher impact angles are shown in Figure 10b. By comparing the Ra value, the results were in good agreement with the SEM images. The critical angle, not the impact angle of the impinging particle, was produced by the effective angle formed by the particle's leading face with the target surface. Only when the particle's orientation at impact produced an effective angle greater than the essential angle for cutting did cutting occur. Ploughing caused a wave of distorted material to be pushed in front of the sliding particle.

The eroded surfaces of the coated specimens at a lower water jet velocity are shown in Figure 11a. Figure 11b illustrates the surface profilometry of the coated specimens at a higher water jet velocity, indicating that the coating deformed plastically at first, but as erosion progressed, the presence of the WC prevented continued plastic flow. Erosion investigations on alloys containing second-phase chromium carbides revealed that the non-uniform nature of the plastic flow caused extremely high strain gradients, resulting in void formation near the chromium carbides and cracking. Once fracture growth reached a critical level, the coatings failed, most likely via spalling, and these processes were thought to be responsible for the material removal. Hence, the high undulations in the coatings were due to the spalling of the coatings. Plastic permanent deformation in the substrate showed lower undulation during the measurement.

Atomic microscopic analysis was also carried out on the uncoated and coated eroded specimens' top surface at low and high velocity. Small trough values were observed at a low velocity in both the uncoated and coated specimens (Figure 11a,b). Particles hitting the surface of a ductile material with a higher velocity than the critical velocity required for permeation eliminate some material. At the impact position on the base material, the particle lost a fraction of its kinetic energy to the destination material in the form of heat and energy in the surface deformation. Extremely high quantities of shear strain could be produced in the material at the moment of impact [52]. Irreversible deformation and larger area spallation of the coatings made large undulations on the coated surface. Hence, the roughness of the coatings' surface increased.

Atomic force microscope images taken at the eroded surface at a low standoff distance are shown in Figure 12a. Figure 12b represents the eroded surface of the coated specimen at a longer standoff distance [53–59]. The small material removal rates at a short standoff distance were due to a decrease in the nozzle pressure as the distance decreased, but the drop in the material removal rate at a longer standoff distance was due to a reduction of the jet velocity as the distance increased. As a result, the value of the standoff distance (Ra) grew and reduced with increasing standoff distance, as seen here.

AFM images of the eroded specimens at low erodent discharge are shown in Figure 13a. The eroded surface at higher erodent discharge is seen in Figure 13b. At all the erodent discharge levels, both the substrate and coatings experienced material loss. Surface profilometry showed the waviness (Ra) was higher [60–65]. The higher Ra level confirmed the material removal from the target surface.

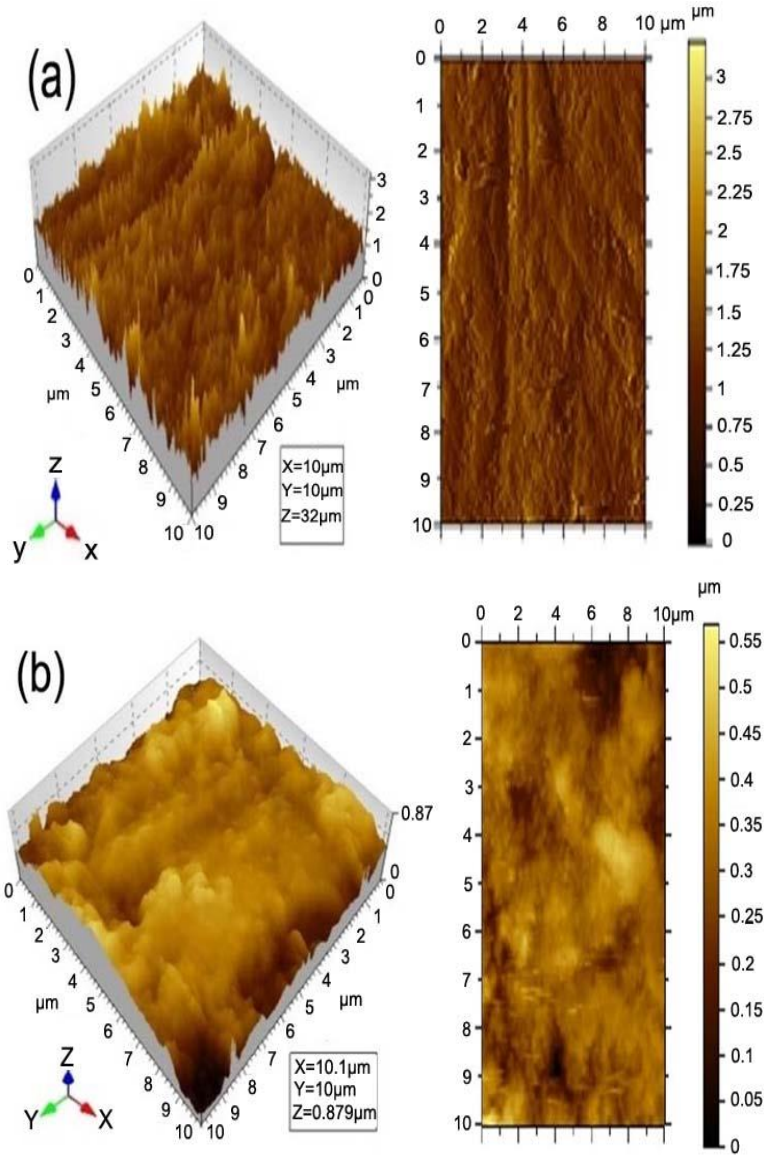

Figure 10. AFM micrographs of the eroded surfaces of the coated specimens at lower and higher impact angles. (**a**) Velocity: 30 m/s, angle: 35°, distance: 45 mm, erodent discharge: 1500 g/min; (**b**) velocity: 50 m/s, angle: 95°, distance: 45 mm, erodent discharge: 1500 g/min.

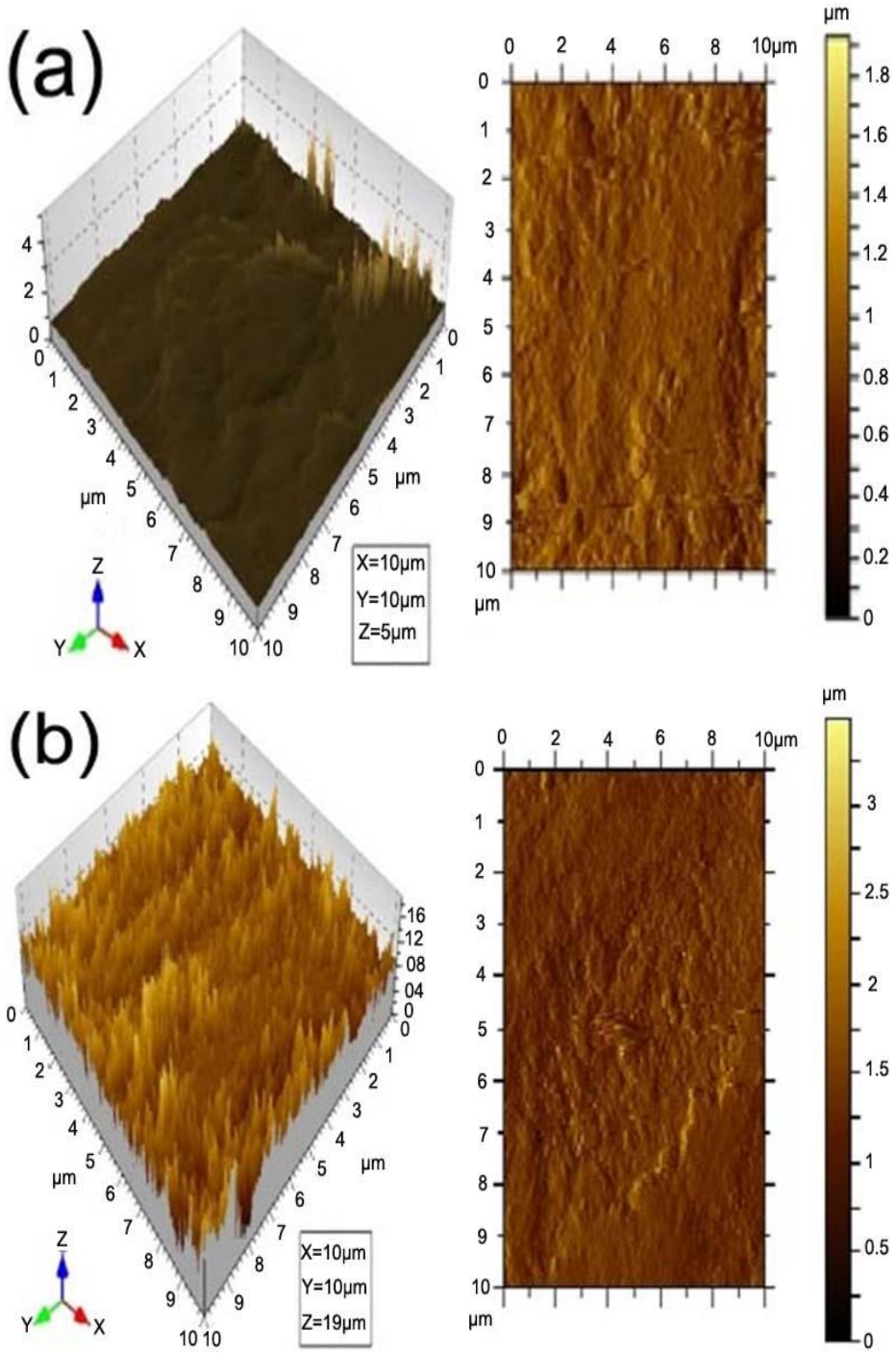

Figure 11. AFM micrographs of the eroded surface of the coated specimens at low and high water jet velocities. (**a**) Velocity: 10 m/s, angle: 60°, distance: 45 mm, erodent discharge: 1500 g/min; (**b**) velocity: 50 m/s, angle: 60°, distance: 45 mm, erodent discharge: 1500 g/min.

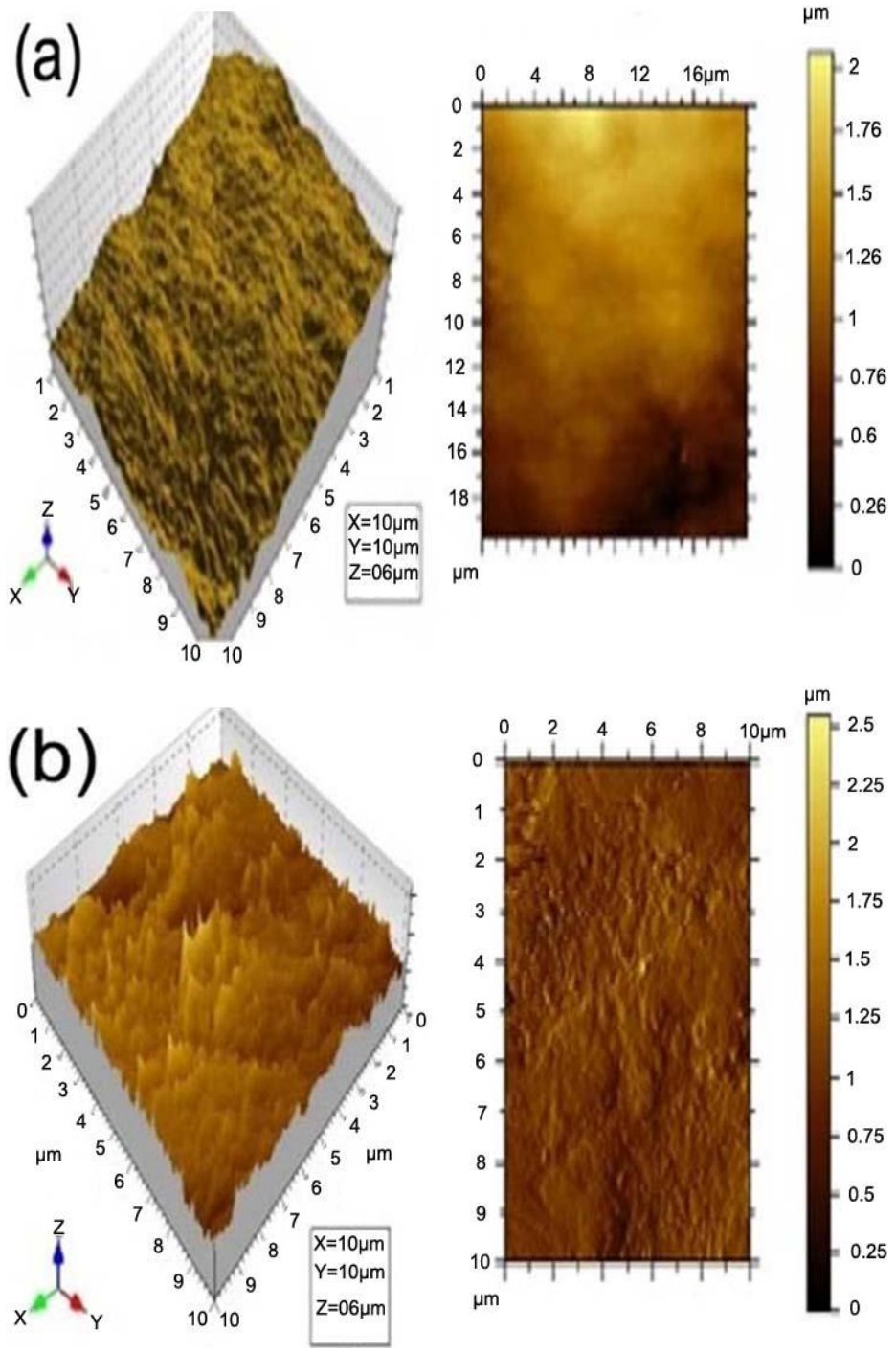

Figure 12. AFM image of the eroded surface of the substrate and coatings at low and high standoff distances. (**a**) Velocity: 30 m/s, angle: 60°, distance: 30 mm, erodent discharge: 2500 g/min; (**b**) velocity: 30 m/s, angle: 60°, distance: 50 mm, erodent discharge: 2500 g/min.

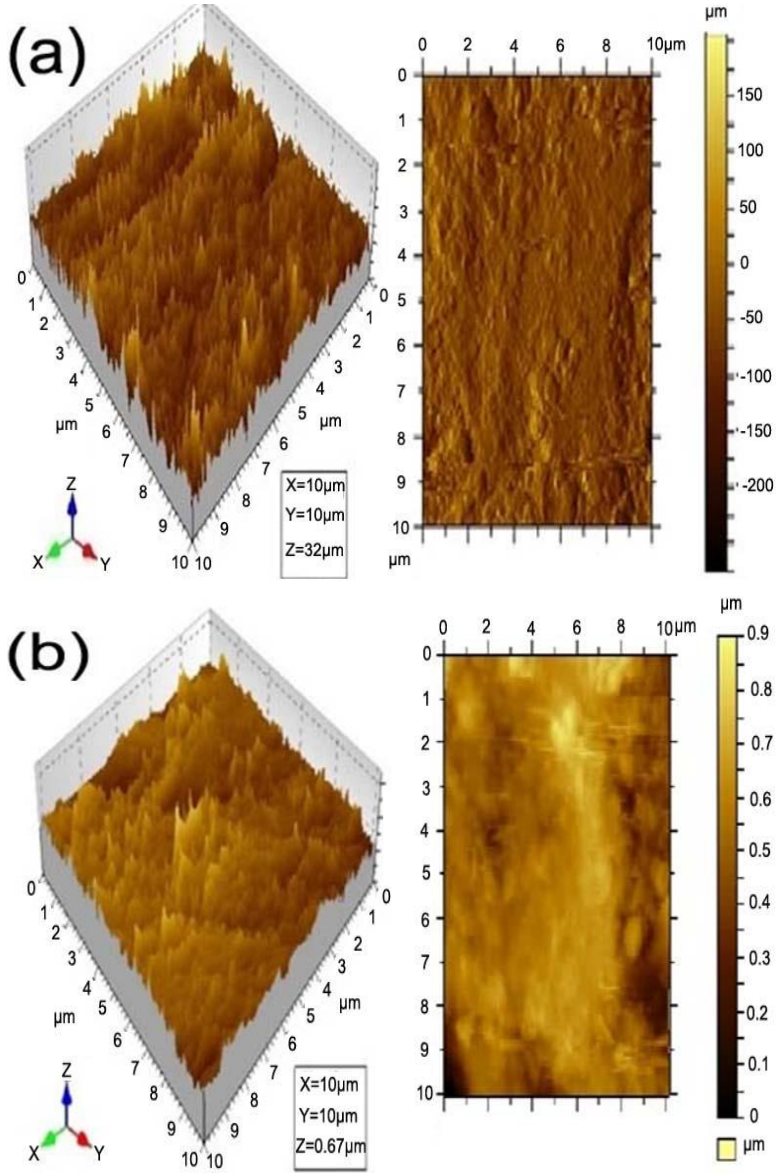

Figure 13. AFM image of the eroded surface of the substrate and coatings at low and high erodent discharge rates. (**a**) Velocity: 30 m/s angle: 60° distance: 55 mm erodent discharge: 500 g/min; (**b**) velocity: 30 m/s angle: 60° distance: 55 mm erodent discharge: 2500 g/min.

The nature of particle–particle interactions is assumed to be separated into two categories: interaction between particles and tubes: the particle–tube interactions occurring from the time the particles are injected into the water stream are thought to decelerate the particles and explain why the particle velocity is lower than the water jet velocity at low flows [66–71].

6. Conclusions

I. The erosion rate of HVOF-sprayed WC-10Co coatings on stainless steel was predicted using an empirical relationship that incorporated the angle of impingement, water jet velocity, standoff distance, and erodent discharge. At a 95% level of confidence, the established correlation can be utilized to estimate the rate of erosion of WC-10Co coatings on stainless steel;

II. The HVOF-sprayed carbide-based coatings showed higher erosion resistance than the uncoated substrate. The coating demonstrated a compact, crack-free coating

with uniform deposition characteristics that were almost equal to the original feedstock powder;

III. Due to the specific mechanical properties of the WC ceramic and consequently high H/E ratio, such coatings are good candidates for protection against water jet erosion;

IV. Among the four process factors studied, the angle of impingement ha the greatest influence on the water jet erosion rate, leading to the water jet velocity, standoff distance, and erodent discharge;

V. At low impact angles (35°), the 35CrMo steel lost more material, and the brittle ceramic-based WC-10Co coatings dissolved at higher angles. The incorporation of the HVOF-sprayed WC-10Cocoating onto the stainless steel resulted in a 40% increase in the water jet erosion resistance.

Author Contributions: Writing-original draft, D.C.R.; Investigation, R.R.; Supervision, D.T.; Writing—review & editing, C.S.R.; Validation, C.A.S.; Resources, A.A.; Review and editing, M.B.; Investigation, B.S. All authors have read and agreed to the published version of the manuscript.

Funding: This research was supported by the Structures and Materials (S&M) Research Lab of Prince Sultan University, and the authors acknowledge the support of Prince Sultan University and King Khalid University for paying the article processing charges (APC) of this publication. The Deanship of Scientific Research at King Khalid University, Saudi Arabia for funding this work through Research Group Program under Grant No: R.G.P.1/104/42. This study is also supported by Taif University Researchers Supporting Project Number (TURSP-2020/49) Taif University, Taif, Saudi Arabia.

Institutional Review Board Statement: Not applicable.

Informed Consent Statement: Not applicable.

Data Availability Statement: Not applicable.

Acknowledgments: The corresponding researcher would like to express his heartfelt gratitude to the Government College of Engineering, Bargur, for providing the coating characterization facilities. S. Sreesabari, Post-Doctoral Scholar, University of Coimbra, Portugal, and R. Paventhan, Dhanalakshmi Srinivasan College of Engineering and Technology, Chennai, Tamilnadu, contributed technical assistance to the authors, which is greatly acknowledged. The authors extend their appreciation to the Deanship of Scientific Research at King Khalid University, Saudi Arabia, for funding this work through the Research Group Program under Grant No. R.G.P.1/104/42. This study wasalso supported by Taif University Researchers Supporting Project Number TURSP-2020/49, Taif University, Taif, Saudi Arabia. The authors would like to thank the Taif University for financial support.

Conflicts of Interest: The authors declare no conflict of interest.

References

1. Khurana, S. Engineering silting problems in hydropower plant. *Int. J. Sci. Res.* **2015**, *4*, 32–33.
2. Roy, M. *Surface Engineering for Enhanced Performance against Wear*; Springer: Friesach, Austria, 2013.
3. Luo, X.; Chidambaram-Seshadri, R.; Yang, G.J. Micro-nanostructured cermet coatings. *Adv. Nano Mater. Coat. Therm. Spray Micro Nano Technol.* **2019**, 61–117. [CrossRef]
4. Miyazaki, N. Solid particle erosion of composite materials: A critical review. *J. Compos. Mater.* **2016**, *50*, 3175–3217. [CrossRef]
5. Vigneshwaran, S.; Uthayakumar, M.; Arumugaprabu, V.; Deepak Joel Johnson, R. Influence of Filler on Erosion Behavior of Polymer Compo-sites: A Comprehensive Review. *J. Reinf. Plast. Compos.* **2018**, *37*, 1011–1019. [CrossRef]
6. Ramachandran, C.S.; Balasubramanian, V.; Ananthapadmanabhan, P.V. Erosion of atmospheric plasma sprayed rare earth oxide coatings under air suspended corundum particles. *Ceram. Int.* **2013**, *39*, 649–672. [CrossRef]
7. Kailash, S.; Praveen, A.S.; Suresh, S.; Sarangan, J.; Murugan, N. Comparison of Microstructural Characteristics of Plasma and HVOF Sprayed Ni-Cr/WC Coating. *Int. J. ChemTech Res.* **2014**, *6*, 3346–3348.
8. Wang, Q.; Zhang, Y.; Ding, X.; Wang, S.; Ramachandran, C.S. Effect of WC Grain Size and Abrasive Type on the Wear Performance of HVOF-Sprayed WC-20Cr_3C_2-7Ni Coatings. *Coatings* **2020**, *10*, 660. [CrossRef]
9. Liu, A.; Guo, M.; Gao, J.; Zhao, M. Influence of bond coat on shear adhesion strength of erosion and thermal resistant coating for carbon fiber reinforced thermosetting polyimide. *Surf. Coat. Technol.* **2006**, *201*, 2696–2700. [CrossRef]
10. Ramachandran, C.S.; Balasubramanian, V.; Ananthapadmanabhan, P.V.; Viswabaskaran, V. Understanding the dry sliding wear behaviour of atmospheric plasma-sprayed rare earth oxide coatings. *Mater. Des.* **2012**, *39*, 234–252. [CrossRef]

11. Ivosevic, M.; Knight, R.; Kalidindi, S.; Palmese, G.; Sutter, J. Solid particle erosion resistance of thermally sprayed functionally graded coatings for polymer matrix composites. *Surf. Coat. Technol.* **2006**, *200*, 5145–5151. [CrossRef]
12. Wang, Q.; Luo, S.; Wang, S.; Wang, H.; Ramachandran, C.S. Wear, erosion and corrosion resistance of HVOF-sprayed WC and Cr3C2 based coatings for electrolytic hard chrome replacement. *Int. J. Refract. Met. Hard Mater.* **2019**, *81*, 242–252. [CrossRef]
13. Matthews, S.; James, B.; Hyland, M. High temperature erosion–oxidation of Cr_3C_2–NiCr thermal spray coatings under simulated turbine conditions. *Corros. Sci.* **2013**, *70*, 203–211. [CrossRef]
14. Rao, Y.; Wang, Q.; Chen, J.; Ramachandran, C.S. Abrasion, sliding wear, corrosion, and cavitation erosion characteristics of a duplex coating formed on AZ31 Mg alloy by sequential application of cold spray and plasma electrolytic oxidation techniques. *Mater. Today Commun.* **2021**, *26*, 101978. [CrossRef]
15. Rao, Y.; Wang, Q.; Oka, D.; Ramachandran, C.S. On the PEO treatment of cold sprayed 7075 aluminum alloy and its effects on mechanical, corrosion and dry sliding wear performances thereof. *Surf. Coat. Technol.* **2019**, *383*, 125271. [CrossRef]
16. Cernuschi, F.; Lorenzoni, L.; Capelli, S.; Guardamagna, C.; Karger, M.; Vaßen, R.; von Niessen, K.; Markocsan, N.; Menuey, J.; Giolli, C. Solid particle erosion of thermal spray and physical vapour deposition thermal barrier coatings. *Wear* **2011**, *271*, 2909–2918. [CrossRef]
17. Ramachandran, C.S.; Balasubramanian, V.; Varahamoorthy, R.; Babu, S. Effect of abrasive slurry parameters on wear behaviour of cobalt-based (stellite) plasma transferred arc hardfaced surface. *Int. J. Surf. Sci.* **2008**, *2*, 502–519. [CrossRef]
18. Wood, R.J.K.; Roy, M. Tribology of thermal-sprayed coatings. In *Surface Engineering for Enhanced Performance against Wear*; Roy, M., Ed.; Print Force: Culemborg, The Netherlands; Springer: Friesach, Austria, 2013; pp. 1–43.
19. Bao, L.; Kameel, H.; Kemmochi, K. Effects of fiber orientation angles of fiber-reinforced plastic on sand solid particle erosion behaviors. *Adv. Compos. Mater.* **2016**, *25*, 81–93. [CrossRef]
20. Mathias, P.; Wu, W.; Goretta, K.; Routbort, J.; Groppi, D.; Karasek, K. Solid particle erosion of a graphite-fiber-reinforced bismaleimide polymer composite. *Wear* **1989**, *135*, 161–169. [CrossRef]
21. Khurana, S.; Varun; Kumar, A. Effect of silt particles on erosion of Turgo impulse turbine blades. *Int. J. Ambient Energy* **2013**, *35*, 155–162. [CrossRef]
22. Finne, I. Erosion of surfaces by solid particles. *Wear* **1960**, *3*, 87–103. [CrossRef]
23. Bitter, J. A study of erosion phenomena: Part II. *Wear* **1963**, *6*, 169–190. [CrossRef]
24. Amarendra, H.J.; Kalhan, P.; Chaudhari, G.P.; Nath, S.K.; Kumar, S. Slurry Erosion Response of Heat Treated 13Cr-4Ni Martensitic Stainless Steel. *Mater. Sci. Forum* **2012**, *710*, 500–505. [CrossRef]
25. Kishor, B.; Chaudhari, G.; Nath, S. Slurry erosion of thermo-mechanically processed 13Cr4Ni stainless steel. *Tribol. Int.* **2016**, *93*, 50–57. [CrossRef]
26. Prasad, R.V.; Rajesh, R.; Thirumalaikumarasamy, D.; Vignesh, S.; Sreesabari, S. Sensitivity analysis and optimisation of HVOF process inputs to reduce porosity and maximise hardness of WC-10Co-4Cr coatings. *Sādhanā* **2021**, *46*, 149. [CrossRef]
27. Katranidis, V.; Gu, S.; Allcock, B.; Kamnis, S. Experimental study of high velocity oxy-fuel sprayed WC-17Co coatings applied on complex geometries. Part A: Influence of kinematic spray parameters on thickness, porosity, residual stresses and microhardness. *Surf. Coat. Technol.* **2017**, *311*, 206–215. [CrossRef]
28. Sapate, S.G.; Tangselwar, N.; Paul, S.N.; Rathod, R.C.; Mehar, S.; Gowtam, D.S.; Roy, M. Effect of Coating Thickness on the Slurry Erosion Resistance of HVOF-Sprayed WC-10Co-4Cr Coatings. *J. Therm. Spray Technol.* **2021**, *30*, 1–15. [CrossRef]
29. Bhandari, S.; Singh, H.; Kumar, S.; Rastogi, V. Slurry Erosion Performance Study of Detonation Gun-Sprayed WC-10Co-4Cr Coatings on CF8M Steel Under Hydro-Accelerated Conditions. *J. Therm. Spray Technol.* **2012**, *21*, 1054–1064. [CrossRef]
30. Kumar, R.E.; Kamaraj, M.; Seetharamu, S.; Kumar, S.A. A pragmatic approach and quantitative assessment of silt erosion characteristics of HVOF and HVAF processed WC-CoCr coatings and 16Cr5Ni Steel for hydro turbine ap-plications. *Mater. Des.* **2017**, *132*, 79–95.
31. Thakur, L.; Arora, N. A comparative study on slurry and dry erosion behaviour of HVOF sprayed WC-CoCr coatings. *Wear* **2013**, *303*, 405–411. [CrossRef]
32. Vignesh, S.; Balasubramanian, V.; Sridhar, K.; Thirumalaikumarasamy, D. Slurry Erosion Behavior of HVOF-Sprayed Amorphous Coating on Stainless Steel. *Met. Microstruct. Anal.* **2019**, *8*, 462–471. [CrossRef]
33. Thakur, L.; Arora, N.; Jayaganthan, R.; Sood, R. An investigation on erosion behavior of HVOF sprayed WC-CoCr coatings. *Appl. Surf. Sci.* **2011**, *258*, 1225–1234. [CrossRef]
34. Wu, Y.; Hong, S.; Zhang, J.; He, Z.; Guo, W.; Wang, Q.; Li, G. Microstructure and cavitation erosion behavior of WC-Co-Cr coating on 1Cr18Ni9Ti stainless steel by HVOF thermal spraying. *Int. J. Refract. Met. Hard Mater.* **2012**, *32*, 21–26. [CrossRef]
35. Daniel, C.; Ribu, R.; Rajesh, D.; Thirumalaikumarasamy, S. Vignesh Influence of rotational speed, angle of impingement, concentration of slurry and exposure time on erosion performance of HVOF sprayed cermet coatings on 35CrMo steel. *Mater. Today Proc.* **2021**, *46*, 7518–7530.
36. Ahmed, R.; Vourlias, G.; Algoburi, A.; Vogiatzis, C.; Chaliampalias, D.; Skolianos, S.; Berger, L.-M.; Paul, S.; Faisal, N.H.; Toma, F.-L.; et al. Comparative Study of Corrosion Performance of HVOF-Sprayed Coatings Produced Using Conventional and Suspension WC-Co Feedstock. *J. Therm. Spray Technol.* **2018**, *27*, 1579–1593. [CrossRef]
37. Mi, P.; Ye, F. Structure and wear performance of the atmospheric heat-treated HVOF sprayed bimodal WC-co coating. *Int. J. Refract. Met. Hard Mater.* **2018**, *76*, 185–191. [CrossRef]

38. *ASTM B276-05*; Standard Test Method for Apparent Porosity in Cemented Carbides. American Society for Testing and Materials: West Conshohocken, PA, USA, 2010.
39. *ASTM C633-01*; Standard Test Method for Tensile Adhesion or Cohesion Strength of Thermal Spray Coatings. American Society for Testing and Materials: West Conshohocken, PA, USA, 2008.
40. *ASTM G75-07 Standard*; Standard Test Method for Determination of Slurry Abrasivity and Slurry Abrasion Response of Materials. American Society for Testing and Materials: West Conshohocken, PA, USA, 2007.
41. Shanmugam, D.T.; Balasubramanian, V. Establishing empirical relationships to predict poros-ity level and corrosion rate of atmospheric plasma sprayed alumina coatings on AZ31B magnesium alloy. *J. Magnes. Alloy.* **2014**, *2*, 140–153.
42. Benyounis, K.; Olabi, A.G.; Hashmi, M. Multi response optimization of CO_2 laserwelding process of austenitic stainless steel. *Opt. Laser Technol.* **2008**, *40*, 76–87. [CrossRef]
43. Al-Bukhaiti, M.; Ahmed, S.; Badran, F.; Emara, K. Effect of impingement angle on slurry erosion behaviour and mechanisms of 1017 steel and high-chromium white cast iron. *Wear* **2007**, *262*, 1187–1198. [CrossRef]
44. Nandre, B.D.; Desale, G.R. Study the Effect of Impact Angle on Slurry Erosion Wear of Four Different Ductile Materials. *Mater. Today Proc.* **2018**, *5*, 7561–7570. [CrossRef]
45. Hutchings, I.M. Normal impact of metal projectiles against a rigid target at low velocities. *Int. J. Mech. Sci.* **1981**, *23*, 255–261. [CrossRef]
46. Babu, A.; Perumal, G.; Arora, H.S.; Grewal, H.S. Enhanced slurry and cavitation erosion resistance of deep cryogenically treated thermal spray coatings for hydroturbine applications. *Renew. Energy* **2021**, *180*, 1044–1055. [CrossRef]
47. Venter, A.M.; Luzin, V.; Marais, D.; Sacks, N.; Ogunmuyiwa, E.N.; Shipway, P.H. Interdependence of slurry erosion wear performance and residual stress in WC-12wt.% Co and WC-10wt.% VC-12wt.% Co HVOF coatings. *Int. J. Refract. Met. Hard Mater.* **2019**, *87*, 105101. [CrossRef]
48. Ludwig, G.A.; Malfatti, C.; Schroeder, R.M.; Ferrari, V.Z.; Muller, I.L. WC10Co4Cr coatings deposited by HVOF on martensitic stainless steel for use in hydraulic turbines: Resistance to corrosion and slurry erosion. *Surf. Coat. Technol.* **2019**, *377*, 124918. [CrossRef]
49. Santacruz, G.; Takimi, A.S.; De Camargo, F.V.; Bergmann, C.P.; Fragassa, C. Comparative Study of Jet Slurry Erosion of Martensitic Stainless Steel with Tungsten Carbide HVOF Coating. *Metals* **2019**, *9*, 600. [CrossRef]
50. NoorbakhshNezhad, A.H.; MohammadiZahrania, E.; Alfantazi, A.M. Erosion-corrosion of electrodeposited superhydrophobic Ni-Al_2O_3nanocomposite coatings under jet saline-sand slurry impingement. *Corros. Sci.* **2022**, *1978*, 110095. [CrossRef]
51. Hong, S.; Wu, Y.; Zhang, J.; Zheng, Y.; Zheng, Y.; Lin, J. Synergistic effect of ultrasonic cavitation erosion and corrosion of WC-CoCr and FeCrSiBMn coatings prepared by HVOF spraying. *Ultrason. Sonochem.* **2016**, *31*, 563–569. [CrossRef] [PubMed]
52. Souza, V.A.D.; Neville, A. Corrosion and erosion damage mechanisms during erosion-corrosion of WC-Co-Cr cermet Coatings. *Wear* **2003**, *255*, 146–156. [CrossRef]
53. Afzal, A.; Samee, A.D.M.; Javad, A.; Shafvan, S.A.; Ajinas, P.V.A.; Kabeer, K.M.A. Heat transfer analysis of plain and dimpled tubes with different spacings. *Heat Transf.-Asian Res.* **2017**, *47*, 556–568. [CrossRef]
54. Soudagar, M.E.M.; Afzal, A.; Safaei, M.R.; Manokar, A.M.; El-Seesy, A.I.; Mujtaba, M.A.; Samuel, O.D.; Badruddin, I.A.; Ahmed, W.; Shahapurkar, K.; et al. Investigation on the effect of cottonseed oil blended with different percentages of octanol and suspended MWCNT nanoparticles on diesel engine characteristics. *J. Therm. Anal.* **2020**, *147*, 525–542. [CrossRef]
55. Soudagar, M.E.M.; Afzal, A.; Kareemullah, M. Waste coconut oil methyl ester with and without additives as an alternative fuel in diesel engine at two different injection pressures. *Energy Sources Part A Recover. Util. Environ. Eff.* **2020**, 1–19. [CrossRef]
56. Verma, T.N.; Nashine, P.; Chaurasiya, P.K.; Rajak, U.; Afzal, A.; Kumar, S.; Singh, D.V.; Azad, A.K. The effect of ethanol-diesel-biodiesel blends on combustion, performance and emissions of a direct injection diesel engine. *Sustain. Energy Tech-Nologies Assess.* **2020**, *42*, 100851. [CrossRef]
57. Afzal, A.; Aabid, A.; Khan, A.; Khan, S.A.; Rajak, U.; Verma, T.N.; Kumar, R. Response surface analysis, clustering, and random forest regression of pressure in suddenly expanded high-speed aerodynamic flows. *Aerosp. Sci. Technol.* **2020**, *107*, 106318. [CrossRef]
58. Afzal, A.; Saleel, C.A.; Badruddin, I.A.; Khan, T.Y.; Kamangar, S.; Mallick, Z.; Samuel, O.D.; Soudagar, M.E. Human thermal comfort in passenger vehicles using an organic phase change material—An experimental investigation, neural network modelling, and optimization. *Build. Environ.* **2020**, *180*, 107012. [CrossRef]
59. Aneeque, M.; Alshahrani, S.; Kareemullah, M.; Afzal, A.; Saleel, C.; Soudagar, M.; Hossain, N.; Subbiah, R.; Ahmed, M. The combined effect of alcohols and *Calophyllum inophyllum* biodiesel using response surface methodology optimization. *Sustainability* **2021**, *13*, 7345. [CrossRef]
60. Afzal, A.; Mokashi, I.; Khan, S.A.; Abdullah, N.A.; Bin Azami, M.H. Optimization and analysis of maximum temperature in a battery pack affected by low to high Prandtl number coolants using response surface methodology and particle swarm optimization algorithm. *Numer. Heat Transf. Part A Appl.* **2020**, *79*, 406–435. [CrossRef]
61. Praveen, A.S.; Arjunan, A. High-temperature oxidation and erosion of HVOF sprayed NiCrSiB/Al_2O_3 and NiCrSiB/WC-Co coatings. *Appl. Surf. Sci. Adv.* **2022**, *7*, 100191. [CrossRef]
62. Nagaraja, S.; Kodanda, R.; Ansari, K.; Kuruniyan, M.S.; Afzal, A.; Kaladgi, A.R.; Aslfattahi, N.; Saleel, C.A.; Gowda, A.C.; Bindiganavile Anand, P. Influence of Heat Treatment and Reinforcements on Tensile Characteristics of Aluminium Aa 5083/Silicon Carbide/Fly Ash Composites. *Materials* **2021**, *14*, 5261. [CrossRef]

63. Chairman, C.A.; Ravichandran, M.; Mohanavel, V.; Sathish, T.; Rashedi, A.; Alarifi, I.M.; Badruddin, I.A.; Anqi, A.E.; Afzal, A. Mechanical and Abrasive Wear Performance of Titanium Di-Oxide Filled Woven Glass Fibre Reinforced Polymer Composites by Using Taguchi and Edas Approach. *Materials* **2021**, *14*, 5257. [CrossRef]
64. Akhtar, M.N.; Khan, M.; Khan, S.A.; Afzal, A.; Subbiah, R.; Bakar, E.A. Determination of Non-Recrystallization Temperature for Niobium Microalloyed Steel. *Materials* **2021**, *14*, 2639. [CrossRef]
65. Sharath, B.N.; Venkatesh, C.V.; Afzal, A. Multi Ceramic Particles Inclusion in the Aluminium Matrix and Wear Characterization through Experimental and Response Surface-Artificial Neural Networks. *Materials* **2021**, *14*, 2895. [CrossRef]
66. Kaur, M.; Singh, H.; Prakash, S. Surface engineering analysis of detonation-gun sprayed Cr_3C_2–NiCr coating under high-temperature oxidation and oxidation–erosion environments. *Surf. Coat. Technol.* **2011**, *206*, 530–541. [CrossRef]
67. Sathish, T.; Mohanavel, V.; Arunkumar, T.; Raja, T.; Rashedi, A.; Alarifi, I.M.; Badruddin, I.A.; Algahtani, A.; Afzal, A. Investigation of Mechanical Properties and Salt Spray Corrosion Test Parameters Optimization for Aa8079 with Reinforcement of Tin + Zro2. *Materials* **2021**, *14*, 5260. [CrossRef] [PubMed]
68. Nagaraja, S.; Nagegowda, K.U.; Kumar, V.A.; Alamri, S.; Afzal, A.; Thakur, D.; Kaladgi, A.R.; Panchal, S.; Saleel, C.A. Influence of the Fly Ash Material Inoculants on the Tensile and Impact Characteristics of the Aluminum AA 5083/7.5SiC Composites. *Materials* **2021**, *14*, 2452. [CrossRef] [PubMed]
69. Rethnam, G.S.N.; Manivel, S.; Sharma, V.K.; Srinivas, C.; Afzal, A.; Razak, R.K.A.; Alamri, S.; Saleel, C.A. Parameter Study on Friction Surfacing of AISI316Ti Stainless Steel over EN8 Carbon Steel and Its Effect on Coating Dimensions and Bond Strength. *Materials* **2021**, *14*, 4967. [CrossRef] [PubMed]
70. Jeevan, T.P.; Jayaram, S.R.; Afzal, A.; Manzoore, H.S.A.; Soudagar, E.M. Machinability of AA6061 Aluminum Alloy and AISI 304L Stainless Steel Using Nonedible Vegetable Oils Applied as Minimum Quantity Lubrication. *J. Brazilian Soc. Mech. Sci. Eng.* **2021**, *43*, 159. [CrossRef]
71. Sathish, T.; Mohanavel, V.; Ansari, K.; Saravanan, R.; Karthick, A.; Afzal, A.; Alamri, S.S. Synthesis and Characterization of Mechanical Properties and Wire Cut EDM Process Parameters Analysis in AZ61. *Materials* **2021**, *14*, 3689. [CrossRef]